ChemComm

COMMUNICATION

View Article Online
View Journal | View Issue

Cite this: *Chem. Commun.*, 2024, **60**, 14617

Received 14th October 2024,
Accepted 13th November 2024

DOI: 10.1039/d4cc05422a

rsc.li/chemcomm

Amorphous Fe–O–P electro(pre)catalysts for energy-efficient H_2 production coupled with ethylene glycol oxidation†

Feifei Yuan,[ac] Xiaoli Chen,[a] Wenhui Yang,[a] Wanting Wu,[a] Manjie Zheng,[a] Jun Xu,[b]* Nan Yu*[c] and Liyong Chen*[ad]

This study presents the synthesis and electrocatalytic performance of amorphous Fe–O–P nanocages derived from Fe-MOFs for water and ethylene glycol (EG) oxidation. Despite structural and compositional changes, the electrocatalyst in an electrolytic cell with Pt/C shows high activity and reduced cell voltage, efficiently generating H_2 and formic acid in a KOH–EG mixed electrolyte.

Hydrogen (H_2), known for its high energy density and sustainability, is a key green source of energy, making it an appealing option to replace fossil fuels for reducing greenhouse gas emissions and combatting climate change with various applications, including fuel cells, industrial processes, and transportation.[1] Water splitting *via* electrocatalysis presents an economically viable and environmentally friendly method for H_2 production.[2] However, during water electrolysis, the slow kinetics of the water oxidation reaction due to its multiple-electron transfer steps with a high energy barrier often become the primary bottleneck, limiting the hydrogen evolution reaction (HER) rate and increasing energy consumption.[3] To address this issue, in addition to developing efficient electrocatalysts for water oxidation, a promising approach is to explore low-potential oxidation half-reactions that can replace water oxidation, thereby reducing energy consumption and improving H_2 production efficiency.[4] The oxidation of small organic molecules is one such alternative, providing a more energy-efficient process for green H_2 production along with value-added chemical byproducts.[5] Among various small organic molecules, ethylene glycol is an attractive, non-toxicity liquid organic molecule that can be produced from renewable biomass through high efficiency processes, and the ethylene glycol oxidation reaction (EGOR) *via* electrocatalysis has been widely studied for fuel cells.[6] In our case, we choose the EGOR as the oxidation half-reaction to replace water oxidation, coupling it with the HER for H_2 production with low energy consumption.

In contrast to crystalline materials, amorphous metal compounds are metastable and feature short-range order with long-range disorder, possibly resulting in more active sites and more favourable electronic structures for electrocatalysis.[7] Herein, we have developed a solution-based method to successfully prepare amorphous Fe–O–P (a-Fe–O–P) nanocages through the phosphorization of spindle-shaped Fe-MOFs (MIL-88A). During the electrocatalytic process, despite the leaching of P and collapse of the nanocages, the resulting iron oxyhydroxide ($FeO_x(OH)_y$),[8] which served as the true active electrocatalyst, exhibited high performance in both the electrocatalytic water oxidation reaction and the EGOR. The enhanced performance may be attributed to defect-enriched $FeO_x(OH)_y$ with a large number of surface unsaturated sites for easy reactant adsorption. Compared to water splitting, the cell voltage for the EGOR coupled with the HER in a two-electrode electrolyzer decreased from 1.60 V to 1.50 V at a current density of 50 mA/cm^2, revealing an energy-saving route for H_2 generation, as well as for formic acid.

Spindle-shaped Fe-MOFs were prepared by a sophisticated synthetic strategy.[9] The crystal structure and morphology of Fe-MOFs were clearly revealed by the X-ray diffraction (XRD) pattern (Fig. S1, ESI†), transmission electron microscopy (TEM) image and field emission scanning electron microscopy (FE-SEM) images at different magnifications (Fig. S2, ESI†), signifying the formation of the spindle-shaped Fe-MOFs. The aspect ratio of the spindle shapes was approximately 5 : 1 with an average length of ~2 μm. The as-prepared Fe-MOFs were further treated with sodium hypophosphite ($NaH_2PO_2{\cdot}H_2O$) in a water–dimethylformamide mixed solvent. During the phosphorization process,

[a] *Department of Pharmaceutical Engineering, Bengbu Medical University, Bengbu, 233030, China. E-mail: lychen@bbmc.edu.cn*
[b] *Department of Physics, Research Institute for Biomimetics and Soft Matter, Fujian Provincial Key Laboratory for Soft Functional Materials, Xiamen University, Xiamen, 361005, China. E-mail: xujun@xmu.edu.cn*
[c] *Anhui Laboratory of Molecule-Based Materials, College of Chemistry and Materials Science, Anhui Normal University, Wuhu, 241002, China. E-mail: yn2009@ahnu.edu.cn*
[d] *Anhui Provincial Key Laboratory of Tumour Evolution and Intelligent Diagnosis and Treatment, Bengbu Medical University, China*

† Electronic supplementary information (ESI) available. See DOI: https://doi.org/10.1039/d4cc05422a

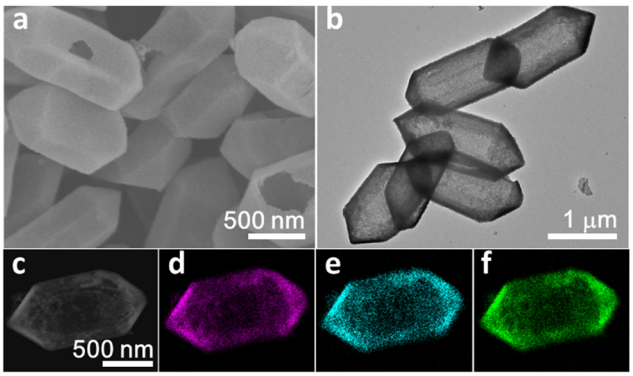

Fig. 1 The as-synthesized a-Fe–O–P microstructures: (a) FE-SEM image, (b) TEM image, (c) STEM image and the corresponding elemental mappings of (d) Fe, (e) P and (f) O.

the spindle shapes gradually transformed into hollow spindle structures that were composed of many tiny nanoparticles, as confirmed by FE-SEM and TEM images (Fig. 1a and b). The distinguished diffraction peaks in the XRD pattern could not be observed (Fig. S3, ESI†). Meanwhile, the clear lattice fringes were not found in the high-resolution TEM (HR-TEM) image (Fig. S4, ESI†), and only a diffraction halo was present in the corresponding selected area electron diffraction (SAED) pattern (inset of Fig. S4, ESI†). These observations indicate that the phosphorized sample has an amorphous structure.[10]

To gain deeper insight into the amorphous sample, elemental mapping was conducted. In the scanning and transmission electron microscopy (STEM) image of the hollow spindle-shaped agglomerate (Fig. 1c), the Fe and P elements were observed to be uniformly distributed across the entire agglomerate (Fig. 1d and e). Interestingly, the presence of the O element was also detected (Fig. 1f), suggesting the incorporation of O into the structure. Therefore, the amorphous sample was identified as the a-Fe–O–P compound. X-ray photoelectron spectroscopy (XPS) was performed to analyse the chemical states of these elements. The high-resolution Fe 2p core-level XPS spectrum of a-Fe–O–P (Fig. S5a, ESI†) showed two dominant peaks at 711.1 and 713.7 eV, corresponding to the two Fe^{3+} $2p_{3/2}$ doublet peaks. A similar pattern of multiplet peaks for Fe^{3+} and Fe^{2+} species have been previously observed in the fitted Fe 2p XPS spectra.[11] In addition, the Fe^{3+} $2p_{1/2}$ peak with a binding energy of 724.9 eV, along with satellite peaks, also appeared in the deconvoluted Fe 2p XPS spectrum. In contrast, no significant change was observed in the Fe 2p core-level XPS spectrum of the Fe-MOF before phosphorization (Fig. S5b, ESI†), further confirming that the Fe species in the a-Fe–O–P sample is assigned to Fe^{3+}. The absence of lower binding energies in the Fe $2p_{3/2}$ spectrum indicates that Fe-P is not present in the Fe–O–P sample. The high-resolution P 2p XPS spectrum of a-Fe–O–P shows a peak at 133.1 eV (Fig. S5c, ESI†), corresponding to P–O bonds, while no lower binding energy peaks associated with Fe–P are observed,[12] further suggesting the formation of Fe–O–P structures. Generally, in the high-resolution XPS spectrum, O 1s are complex. In this study, two peaks are needed to fit the O 1s XPS broadband for the Fe–O–P sample (Fig. S5d, ESI†). These peaks at 529.9 and 531.4 eV were attributed to O from oxide ions and surface hydroxyl (OH) groups,[13] respectively.

The electrocatalytic activity of all electrodes for the oxygen evolution reaction (OER) was assessed after activation by cyclic voltammetry, conducted at a scan rate of 100 mV s^{-1} for 50 cycles. Linear sweep voltammetry (LSV) measurements, performed at a scan rate of 5 mV s^{-1} in a 1.0 M KOH solution, demonstrate that the a-Fe–O–P loaded Ni foam (a-Fe–O–P/NF) exhibits superior electrocatalytic activity for the OER in a standard three-electrode system, compared to other electrodes, including Fe-MOF loaded NF (Fe-MOF/NF) and commercial RuO_2 loaded NF (RuO_2/NF) (Fig. 2a). For example, at different current densities of 10, 50, 100, and 200 mA cm^{-2}, the a-Fe–O–P/NF electrode consistently exhibited the lowest overpotentials (271, 304, 326, and 338 mV, respectively) among all tested electrodes (Fig. 2a). Bare NF, as a support electrode, exhibited a negligible current density (Fig. 2a), indicating that the enhanced catalytic activity for the OER originates from RuO_2 and the as-prepared electrocatalysts. In comparison with previously reported electrocatalysts for the OER in alkaline solutions, the a-Fe–O–P/NF electrode exhibits comparable or even superior electrocatalytic activity (Table S1, ESI†). The cycling stability and durability of electrocatalysts are an important indicator of their electrocatalytic performance. The a-Fe–O–P/NF electrode showed an LSV curve after 1000 cycles that was similar to the curve before cycling (Fig. 2c), suggesting that the a-Fe–O–P/NF electrode has excellent cycling stability. Chronopotentiometry is a useful method for assessing the durability of electrocatalysts. In this study, over the course of 87 h of continuous electrocatalysis at a current density of 50 mA cm^{-2}, the potential only slightly increased from 1.577 to 1.586 V *vs.* RHE according to the chronopotentiometric curve (Fig. 2d). This minimal change in potential reveals the long-term durability of the a-Fe–O–P/NF electrode.

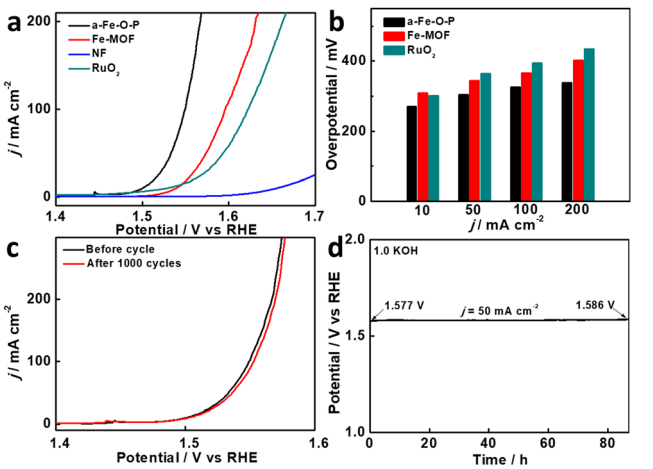

Fig. 2 (a) LSV curves of NF, RuO_2/NF, Fe-MOF/NF, and a-Fe–O–P/NF electrodes in 1.0 M KOH solution, (b) overpotentials at *j* values of 10, 50, 100, and 200 mA cm^{-2}, (c) LSV curves of the a-Fe–O–P/NF electrode before and after 1000 cycles, and (d) chronopotentiometry curve of the a-Fe–O–P/NF electrode at a *j* value of 50 mA cm^{-2} for 86 h.

The oxidation of ethylene glycol presents both economic viability and environmental benefits, positioning it as a promising alternative to the OER in water electrolysis for H_2 production. According to the LSV curves (Fig. 3a), when ethylene glycol was added to the KOH electrolyte solution, the a-Fe–O–P electrocatalyst demonstrated the highest electrocatalytic activity for the EGOR in the three-electrode catalytic system at high potential; in contrast, RuO_2 at low potential showed the largest anodic current density. As shown in Fig. 3b, the potentials at different current densities reveal the same result. The electrocatalytic performance of the a-Fe–O–P electrocatalyst was further measured in a two-electrode system. When EG was added to the KOH electrolyte solution, the Pt/C/NF(−)//Fe–O–P/NF(+) electrolyser showed a lower cell voltage at the same current density in the LSV curves (Fig. 3c). This can be attributed to the replacement of water oxidation by EG oxidation, which is further confirmed by the absence of bubbles at the anode. Formic acid produced from the EGOR was detected by high-performance liquid chromatography (HPLC) (Fig. S6, ESI†). The Faraday efficiency for formic acid at a current density of 50 mA cm^{-2} was ~89.5% during continuous electrocatalysis over 12 h. Hence, the replacement of the OER with the EGOR not only promotes H_2 generation at a lower voltage but also yields value-added products. The durability test was conducted in a mixed solution containing 1.0 M KOH and 0.5 M EG, with the solution being periodically replaced with a fresh one at 12-h intervals. As electrolysis progressed, the current density gradually decreased primarily due to the consumption of EG being oxidized to formic acid; after replacing it with a fresh electrolyte solution, the current density was restored, even after 24 h of continuous catalysis (Fig. 3d), revealing the ultra-stability of electrocatalytic activity.

The long-term durability of electrocatalysts is generally closely related to the stability of their structure and composition. However, in this study, the SEM image (Fig. S7, ESI†) revealed morphological changes in the a-Fe–O–P electrocatalyst for the durability of the EGOR for 36 h, including the collapse of the hollow cage-like structure. Additionally, XPS analysis showed the absence of phosphorus after catalysis (Fig. S8, ESI†). These observations suggest that structural and compositional transformations occur in the amorphous electrocatalyst during the electrocatalytic process. We hypothesize that the actual active species is defect-enriched $FeO_x(OH)_y$, formed through the oxidation of a-Fe–O–P under anodic conditions. Supporting this, the high-resolution Fe 2p XPS spectrum (Fig. S9a, ESI†) revealed minimal changes in Fe^{3+} before and after catalysis, with the exception of a weak broad peak observed in the low binding energy region, consistent with previously reported studies on FeOOH.[14] The clear differences between the O 1s spectra in Fig S5c and S9b (ESI†) confirm the formation of $FeO_x(OH)_y$. The shift of the O 1s peaks to higher binding energies, specifically at 530.4 eV and 532.1 eV after catalysis, can be attributed to the Fe−O and Fe−OH bonds,[15] respectively. Additionally, the peak at 535.5 eV likely originates from adsorbed H_2O molecules.

The reaction kinetics of these NF-supported electrodes was evaluated from Tafel slopes according to the equation $\eta = a + b\log(j)$. Among them, the a-Fe–O–P/NF electrode showed the smallest Tafel slope of 50.5 mV dec^{-1} (Fig. 4a), indicating its superior reaction kinetics for the catalytic OER process. The Nyquist plots of a-Fe–O–P/NF were recorded at different overpotentials to evaluate the electron transfer behaviour between the electrode and the electrolyte (Fig. 4b). The inset of Fig. 4b displays an equivalent circuit, where the R_{ct} represents the charge-transfer resistance, reflecting the electrocatalytic kinetics. As the overpotential increased from 250 to 300 mV, the semicircle diameters of Nyquist plots progressively decreased, indicating a gradual reduction in R_{ct}. This suggests that electron transfer at the electrode–electrolyte interfaces becomes more efficient at higher potentials. In Fig. 4c, the Nyquist plots of bare NF, Fe-MOF/NF, and a-Fe–O–P/NF were recorded at an overpotential of 280 mV in the 1.0 M KOH solution. The a-Fe–O–P/NF electrode exhibited the smallest R_{ct}, as indicated by the smallest semicircle diameter, demonstrating that the a-Fe–O–P structure effectively facilitated electron transfer from the electrode to the electrolyte.

The electrochemical active surface area (ECSA), a crucial parameter for assessing the electrocatalytic activity, was determined by measuring the CV curves of the working electrodes in a non-faradaic region (0.842–0.942 V *vs.* RHE) at varying scan rates of 30, 60, 90, 120, 150, and 180 mV s^{-1} (Fig. S10a–c, ESI†).

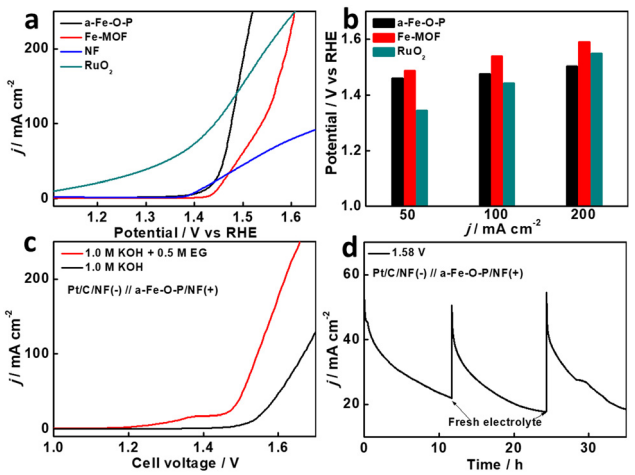

Fig. 3 (a) LSV curves of NF, RuO_2/NF, Fe-MOF/NF, and a-Fe–O–P/NF electrodes in a KOH–EG mixed solution and (b) overpotentials at *j* values of 50, 100, and 200 mA cm^{-2}, (c) LSV curves of Pt/C/NF(−)//a-Fe–O–P/NF(+) in KOH solution with and without EG, and (d) chronoamperometry curve of Pt/C/NF(−)//a-Fe–O–P/NF(+) at 1.58 V with a change of the electrolyte (0.5 M EG and 1.0 M KOH) at an interval of 12 h.

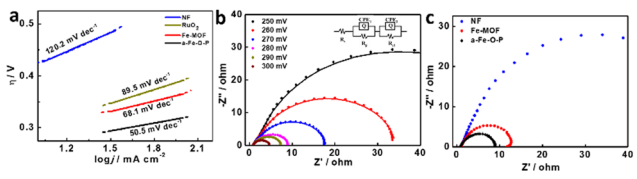

Fig. 4 (a) Tafel plots of different electrodes in 1.0 M KOH solution at a scan rate of 5 mV s^{-1}, (b) Nyquist plots of the a-Fe–O–P/NF electrode recorded at different overpotentials, and (c) Nyquist plots of different electrodes measured at an overpotential of 280 mV.

A linear relationship was observed between the scan rates and the $\Delta j/2$ (where $\Delta j = j_{anodic} - j_{cathodic}$) values at 0.892 V (*vs.* RHE) for the a-Fe–O–P/NF, Fe-MOF/NF, and NF electrodes. In contrast to the Fe-MOF/NF electrode, the a-Fe–O–P/NF electrode shows a higher double-layer capacitance (C_{dl}) value, as indicated by their respective slopes (Fig. S10d, ESI†). The ECSA was calculated using the formula ECSA = C_{dl}/C_s, where C_s represents the specific capacitance (assumed to be 0.040 mF cm^{-2} in the alkaline solution).[16] Based on this calculation, the a-Fe–O–P electrocatalyst demonstrated a higher ECSA compared to both the Fe-MOF electrocatalyst and NF. This increased ECSA can be attributed to its rough surface, which is composed of small nanoparticles with defect-rich structures, providing a significantly larger active surface area than that of Fe-MOFs. These results highlight that the a-Fe–O–P electrocatalyst offers more accessible catalytic sites for the OER/EGOR, thus outperforming its counterparts in terms of electrocatalytic activity.

This study developed a solution-based synthesis strategy to successfully prepare amorphous Fe–O–P nanocages through the phosphorization of Fe-MOFs (MIL-88A). Amorphous materials, characterized by short-range order and long-range disorder, offer abundant active sites, leading to their excellent electrocatalytic performance. The research demonstrated that during the electrocatalytic process, although phosphorus leached and the nanocage structure collapsed, the defect-enriched iron oxyhydroxide ($FeO_x(OH)_y$) served as the actual active species, enhancing the performance of both the OER and the EGOR. Compared to conventional water splitting, coupling the EGOR with the HER reduced the cell voltage from 1.60 V to 1.50 V at a current density of 50 mA cm^{-2}, while producing value-added chemicals such as formic acid. This electrocatalyst also exhibited good cycling stability and long-term durability, making it a promising material for efficient and energy-saving hydrogen production.

The authors acknowledge the financial support from the Natural Science Foundation of Anhui Provincial Department of Education (KJ2021A0730, 2022AH051472, and 2023AH051962), the Academic Program Foundation of Anhui Province for Top Talents of Universities (gxbjZD2022040), the University Synergy Innovation Program of Anhui Province (GXXT-2021-013), the Open Foundation of Anhui Provincial Laboratory of Molecular-Based Materials (fzj22014), and the National Innovation and Entrepreneurship Training Program for College Students (202410367066).

Data availability

The data underlying this study are available in the article and the ESI.†

Conflicts of interest

There are no conflicts to declare.

Notes and references

1 P. Nikolaidis and A. Poullikkas, *Renewable Sustainable Energy Rev.*, 2017, **67**, 597–611.
2 (*a*) J. Zhu, L. Hu, P. Zhao, L. Y. S. Lee and K.-Y. Wong, *Chem. Rev.*, 2020, **120**, 851–918; (*b*) X. Xu, Y. Zhong, M. Wajrak, T. Bhatelia, S. P. Jiang and Z. Shao, *InfoMat*, 2024, **6**, e12608; (*c*) H. Sun, X. Xu, G. Chen and Z. Shao, *Carbon Energy*, 2024, e595.
3 (*a*) C. Hu, L. Zhang and J. Gong, *Energy Environ. Sci.*, 2019, **12**, 2620–2645; (*b*) S. Yu, J. Li, Y. Du, Y. Wang, Y. Zhang and Z. Wu, *Coord. Chem. Rev.*, 2024, **520**, 216144.
4 L. Zeng, Y. Chen, M. Sun, Q. Huang, K. Sun, J. Ma, J. Li, H. Tan, M. Li, Y. Pan, Y. Liu, M. Luo, B. Huang and S. Guo, *J. Am. Chem. Soc.*, 2023, **145**, 17577–17587.
5 (*a*) G. Yang, Y. Jiao, H. Yan, Y. Xie, A. Wu, X. Dong, D. Guo, C. Tian and H. Fu, *Adv. Mater.*, 2020, **32**, 2000455; (*b*) N. Thakur, D. Mehta, A. Chaturvedi, D. Mandal and T. C. Nagaiah, *J. Mater. Chem. A*, 2023, **11**, 15868–15877; (*c*) Y. Wang, W. Yan, M. Ni, C. Zhu and H. Du, *Chem. Commun.*, 2023, **59**, 2485–2488; (*d*) L. Fei, H. Sun, X. Xu, Y. Li, R. Ran, W. Zhou and Z. Shao, *Chem. Eng. J.*, 2023, **471**, 144660; (*e*) J. Yu, Z. Li, C. Wang, X. Xu, T. Liu, D. Chen, Z. Shao and M. Ni, *J. Colloid Interface Sci.*, 2024, **661**, 629–661.
6 (*a*) D. Jang, M. Park, J. Maeng, J. Ha, S. Choi, N. Kim, M. H. Seo and W. B. Kim, *Small*, 2024, 2404540; (*b*) Q. Mao, K. Deng, H. Yu, Y. Xu, Z. Wang, X. Li, L. Wang and H. Wang, *Adv. Funct. Mater.*, 2022, **32**, 2201081; (*c*) J. Li, K. Ji, B. Li, M. Xu, Y. Wang, H. Zhou, Q. Shi and H. Duan, *Angew. Chem., Int. Ed.*, 2023, **62**, e202304852; (*d*) L. Fan, Y. Ji, G. Wang, J. Chen, K. Chen, X. Liu and Z. Wen, *J. Am. Chem. Soc.*, 2022, **144**, 7224–7235; (*e*) N. Zhang, K. Zhang, J. Li, C. Ye and Y. Du, *J. Colloid Interface Sci.*, 2023, **650**, 1509–1517.
7 (*a*) K. Zhang, Q. Su, W. Shi, Y. Lv, R. Zhu, Z. Wang, W. Zhao, M. Zhang, S. Ding, S. Ma, G. Du and B. Xu, *ACS Nano*, 2024, **18**, 3791–3800; (*b*) H. Cheng, N. Yang, G. Liu, Y. Ge, J. Huang, Q. Yun, Y. Du, C. J. Sun, B. Chen, J. Liu and H. Zhang, *Adv. Mater.*, 2020, **32**, 1902964.
8 (*a*) B. You, N. Jiang, X. Liu and Y. Sun, *Angew. Chem., Int. Ed.*, 2016, **55**, 9913–9917; (*b*) R. Beltrán-Suito, P. W. Menezes and M. Driess, *J. Mater. Chem. A*, 2019, **7**, 15749–15756.
9 H. Xu, C. Shan, X. Wu, M. Sun, B. Huang, Y. Tang and C.-H. Yan, *Energy Environ. Sci.*, 2020, **13**, 2949–2956.
10 J. Liu, X. Liu, H. Shi, J. Luo, L. Wang, J. Liang, S. Li, L.-M. Yang, T. Wang, Y. Huang and Q. Li, *Appl. Catal., B*, 2022, **302**, 120862.
11 (*a*) M. Mullet, V. Khare and C. Ruby, *Surf. Interface Anal.*, 2008, **40**, 323–328; (*b*) J. Guo, J. Cao and S. Jia, *Int. J. Electrochem. Sci.*, 2020, **15**, 10524–10540.
12 J. Dong, G. Liu, Y. V. Petrov, Y. Feng, D. Jia, V. E. Baulin, A. Yu Tsivadze, Y. Zhou and B. Li, *Adv. Healthcare Mater.*, 2024, 2402568.
13 J. Yang, H. Liu, W. N. Martens and R. L. Frost, *J. Phys. Chem. C*, 2010, **114**, 111–119.
14 A. N. Mansour and R. A. Brizzolara, *Surf. Sci. Spectra*, 1996, **4**, 357–362.
15 Z. Lin, H. Zhang, G. Liang, Y. Jin, H. Zeng, J. Li, J. Chen, W. Zhang, F. Xie, Y. Jin and H. Meng, *Chem. – Eur. J.*, 2019, **25**, 3112–3118.
16 D. Voiry, M. Chhowalla, Y. Gogotsi, N. A. Kotov, Y. Li, R. M. Penner, R. E. Schaak and P. S. Weiss, *ACS Nano*, 2018, **12**, 9635–9638.

